Chapter 6

# Discharge Behavior of Water-Activated Magnesium Battery

Isao Nakatsugawa, Yasumasa Chino and Hideki Nakano

Additional information is available at the end of the chapter

http://dx.doi.org/10.5772/intechopen.79789

**Abstract**

Water-activated magnesium batteries possess several favorable attributes for energy storage and lighting sources. In this chapter, a portable-sized magnesium battery which consisted of $MnO_2$ cathodes and magnesium alloy anodes, being activated by drops of water, was investigated. The anode and cathode potential as well as their electrochemical impedance under a constant current load was monitored to evaluate the effect of water content, cell stacking, and discharging cycles. It was revealed that the discharge behavior was initially controlled by the depletion of water, followed by the cease of cathode reaction and the accumulation of $Mg(OH)_2$ at anode. The problem of low anode efficiency caused by stacking cells was analyzed, and its countermeasure was proposed. Several approaches to improve the battery performance were also presented.

**Keywords:** magnesium, primary battery, water-activated, electrochemical impedance, $MnO_2$

## 1. Introduction

Magnesium has a negative standard potential of −2.37 V vs. SHE and a high Faradaic capacity of 2.205 Ah/g, which is an attractive feature as the primary battery anode [1]. Mg primary batteries (dry batteries) were successfully used for military applications till 1970s [2]. Water/seawater-activated Mg batteries, or reserved batteries, are preferentially used for undersea devices or emergency signals [3]. Research and development of Mg-ion secondary batteries are under way. Charge-discharge performance comparable to lithium-ion batteries is a challenging task [4, 5]. In recent years, water-activated Mg batteries have been reevaluated [6–8].

Unlike other primary batteries, Mg batteries can be activated with neutral electrolyte when in use. This ensures a long shelf life, easy-to-use operation, and safe disposal of used batteries. Conventional sea water-activated Mg batteries use metal chloride cathodes [1, 3]. Recent water-activated Mg batteries follow the same principle, with incorporating modern electric and battery technologies. There are roughly two kinds of water-activated batteries. Type I battery consists of Mg anode, air-diffusion cathode, and electrolyte container. An appropriate amount of neutral electrolyte, usually NaCl solution, is injected in use. It is also called Mg-air battery [1, 6, 7]. Type II battery is a stacked structure of unit cells, and a small amount of water (1~2 ml) is injected in use [8]. Type I batteries can generate current densities of around tens of mA/cm$^2$ and can be served as small-middle sized generators. Although the capacity of the type II battery is limited (about 1 mA/cm$^2$), it is compact and boosts up easily by stacking unit cells, suitable for power saving devices like LED. There are several articles about type I battery [1, 6, 7], but technical information is limited for type II battery. Hereafter, type II battery is called as water-activated magnesium battery (WAMB) and described in this article.

**Figure 1** shows several WAMB-operated LED lamps and their structure [9]. It is the size of a cigarette lighter, weighs about 20 g. A WAMB contains 3–4 unit cells stacked in a plastic casing. One or two LEDs are connected to the battery terminals. Details of the unit cell will be discussed later. Small amount of water is injected to the bottom of the casing to illuminate LED [10]. In the absence of water, juice and saliva can be used. As water is gradually lost during discharge, its intermittent supply is necessary. **Figure 2** shows the change in LED illuminance with water injection [9]. Comparisons with other illumination sources are mentioned. Each water injection restores illuminance while the intensity gradually disappears. After 6–7 injections, the WAMB cannot generate enough power for the LED and goes out. One WAMB can provide light in about a week, which is sufficient as an emergency illumination source. In addition to its compactness, it does not contain any hazardous substances, which enables safe operation and disposal of the used WAMB [8, 9].

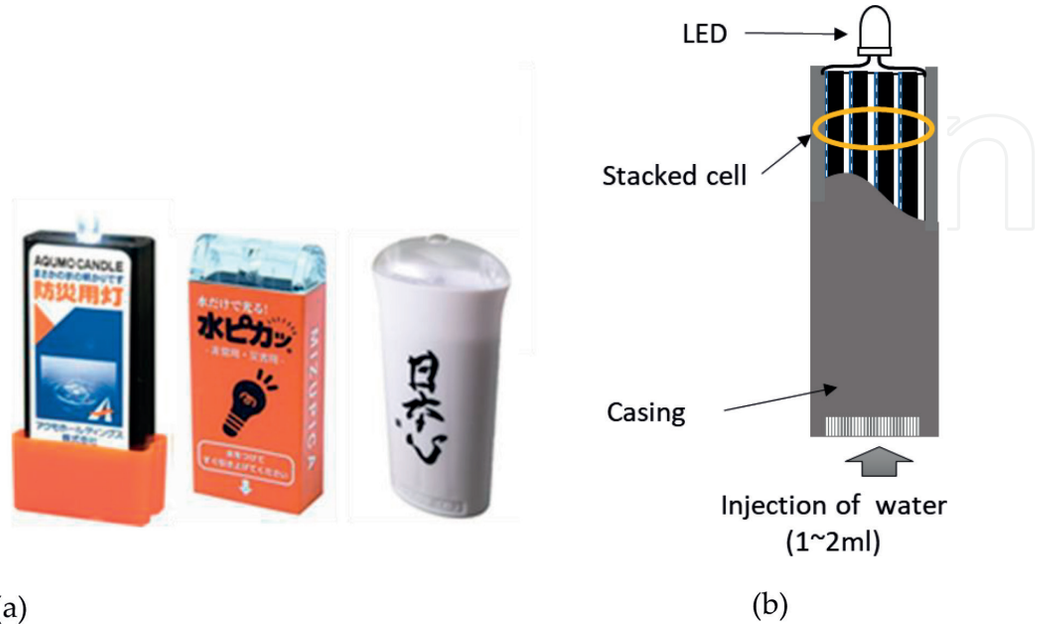


**Figure 1.** Appearance and structure of type II WAMB. (a) Commercial product (handy LED lamp). (b) Structure.

http://dx.doi.org/10.5772/intechopen.79789

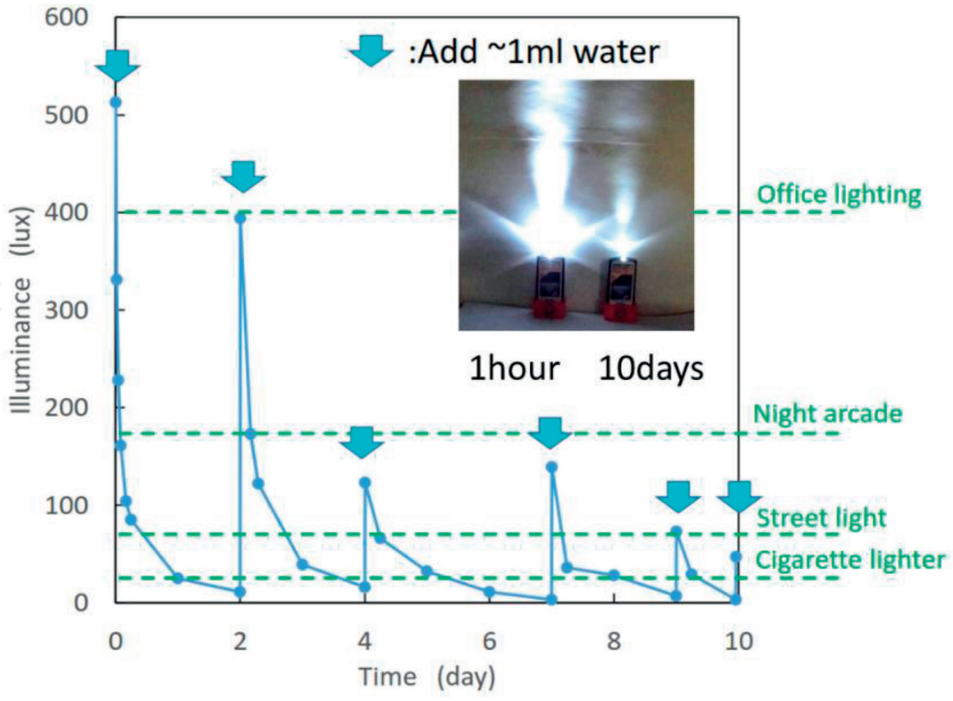


**Figure 2.** Illuminance of WAMB (stacked cell). Illuminance was measured at 30 cm distance from LED [9].

In this chapter, the discharge performance of WAMB is presented based on our recent research [11–13]. We first describe the discharge behavior of unit cells, following the studies of cell stacking. Factors that affect discharge performance are identified and analyzed. Several approaches to improve performance are also proposed.

## 2. Materials and methods

A Mg-3%Al-1%Zn alloy (AZ31) magnesium alloy plate having a thickness of 0.8 mm (manufactured by Osaka Fuji Corp.) was used as the anode. The chemical composition is shown in **Table 1**. The surface was polished with #600 SiC paper, rinsed with water, and wiped with ethanol. As a cathode material, a part of commercially available WAMB (Aqumo Holdings "Aqumo candle®") [9] was used. Although details are not clarified, it seems to consist of pulp-based nonwoven fabric containing $MnO_2$, catalyst, graphite, and NaCl [8]. A Cu foil having a thickness of 0.6 mm was used as the current collector of the cathode. As the separator, pulp/polypropylene nonwoven fabric having a thickness of 0.25 mm was used. These electrodes were piled in the order of current collector/cathode/separator/anode to construct the unit cell, shown in **Figure 3**. The electrode size was 25 × 50 mm except for the separator which had 10 mm longer than others for absorbing water. A Pt wire of ϕ 0.6 mm was sandwiched

| | Al | Zn | Mn | Si | Fe + Cu + Ni | Mg |
|---|---|---|---|---|---|---|
| **AZ31B** | 3.03 | 0.78 | 0.29 | 0.021 | <0.006 | Bal. |

**Table 1.** Chemical composition of the Mg anode.

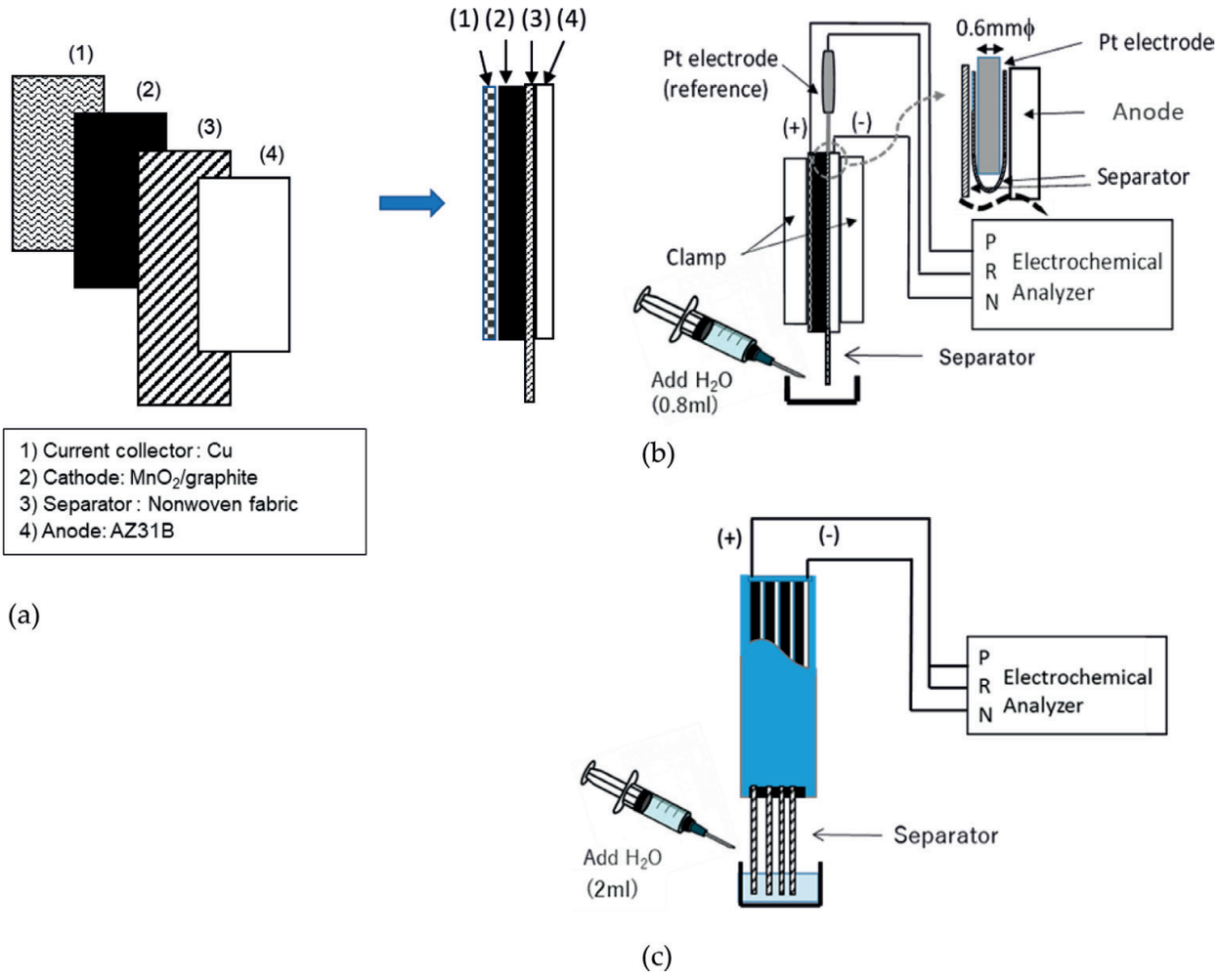


**Figure 3.** Experimental setup of WAMB discharge study. (a) Structure of the unit cell. (b) Setup of the unit cell. (c) Setup of the stacked cell.

between the separator and the anode and used as a reference electrode. To avoid direct contact with the Pt wire, a small piece of the separator was attached to the anode side. Two Cu sheets were attached to the outside of the unit cell and used as terminals. The assembly was further cramped with two acrylic plates under a pressure of 6 N. Stacked cells were prepared by superimposing four unit cells in series and inserted into a commercial WAMB casing. Tap water (Sagami river system, Samukawa water purifying plant) was used to activate WAMB by injecting them into the bottom of the separator. The amount of water was varied from 0.4 to 0.8 ml in a unit cell and 2 ml in a stacked cell.

The initial discharge capacity of WAMB was analyzed with a unit cell by measuring a potentiodynamic polarization curve. After 20 min of water injection, the cell voltage $V_{cell}$ and the discharge current density $i_d$ were monitored at a scanning rate of 1 mV/s.

A constant current discharge test of 0.24 mA/cm$^2$ in the unit cell and 0.08–0.80 mA/cm$^2$ in the stacked cell was performed. The anode potential $E_a$, the cathode potential $E_c$, $V_{cell}$, and electrochemical impedance spectroscopy (EIS) of the anode, cathode, and cell were independently measured in the unit cell. In the stacked cell, $V_{cell}$ and the cell impedance were monitored. The EIS was performed in a current-controlled mode with an amplitude of 1% of $i_d$, and the

scanned frequency was changed from 100 kHz to 1 Hz using an electrochemical apparatus (Solartron Analytical, Modulab Xm). The obtained spectrum was analyzed by curve fitting software (Scribner ZView). When $V_{cell}$ fell below the terminal voltage of 0.7 V in the unit cell and 2.5 V in the stacked cell, the discharge test was interrupted. After that, the same amount of water was injected, and the test was restarted. When $V_{cell}$ decreased to the terminal voltage within 1 h after water injection, the discharge test was terminated, and cumulative discharge time $t_{total}$ (h) was calculated.

The discharge capacity was evaluated by the gravimetric energy density $E_g$ (Wh/kg).

$$E_g = V_{cell.avg} \times i_d \times S \times t_{total}/(M + L) \quad (1)$$

$V_{cell.avg}$ is the average of the monitored $V_{cell}$, $S$ is the area of the electrode (= 12.5 cm$^2$), $M$ is the cell weight (g), and $L$ is the total amount of injecting water (g). $M$ does not include the weight of the casing. For the calculation of Eq. (1), $L$ is fixed as 1.5 g for a unit cell and 6 g for a stacked cell, referring the result of the weight increase after the discharge test.

After the test, the discharged cells were disassembled, and the appearance of the electrodes was examined. The consumption of Mg anode $\Delta W$ (g) was measured after removing the discharged product by a wire brush. Current efficiency $CE$ (%) was calculated by Eq. (2).

$$CE = i_d \times S/I_{grav.} \times 100 \quad (2)$$

$Igrav_.$ (mA) was calculated with $\Delta W$, assuming Mg is dissolved with the ionic valency of 2.

$$I_{grav.} = 2 \times 96{,}500 \times \Delta W/t_{total}/24.31 = 2206\ \Delta W/t_{total} \quad (3)$$

## 3. Results

### 3.1. Initial discharge capacity of unit cell

**Figure 4** shows the polarization curve of the unit cell with a water injection of 0.8 ml [13]. The power density reached about 10 mW/cm$^2$ with $i_d$ of 15 mA/cm$^2$. As described later, the current range used in the constant discharge test was less than 1 mA/cm$^2$ (<10 mA), and $V_{cell}$ was about 1.4 to 1.5 V. By stacking four cells in series, $V_{cell}$ reaches 5.6 ~ 6 V, which is sufficient to illuminate a small LED with a forward voltage of 2.5–3.5 V.

### 3.2. Discharge behavior of unit cell with water injection

**Figure 5(a)** shows the discharge curve of WAMB unit cell at the initial injection of water [11]. The amount of water was changed from 0.4 to 0.8 ml. The unit cell did not hold more than 1 ml of water. $V_{cell}$ was kept at about 1.4 V for a certain period and declined rapidly. The larger the amount of water, the longer the discharge time was obtained. **Figure 5(b)** shows the dependence of the discharge time on the amount of water. A relationship expressed by a quadratic function can be seen. Hereafter, the injection of water was fixed to 0.8 ml.

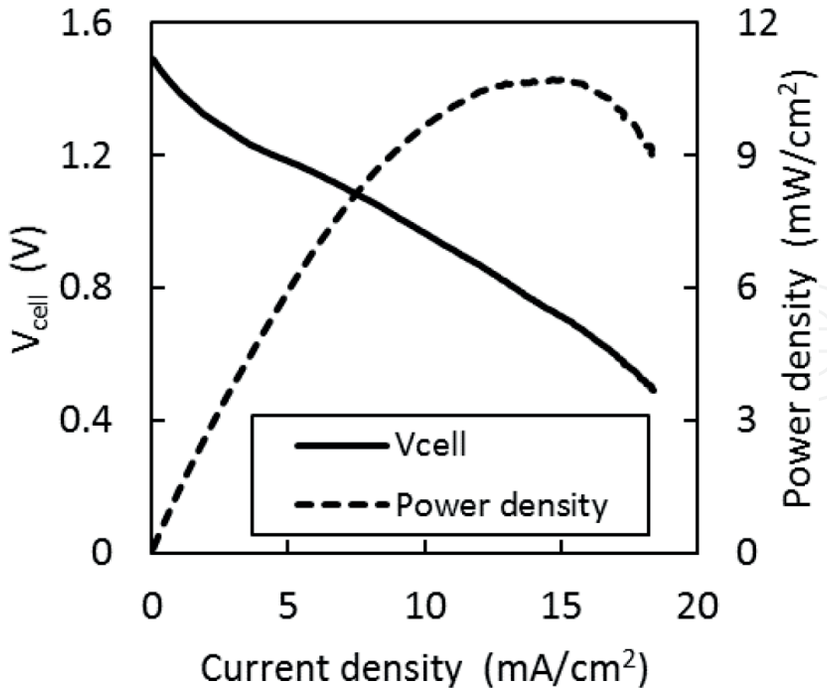


**Figure 4.** Initial discharge performance of WAMB (unit cell) [13].

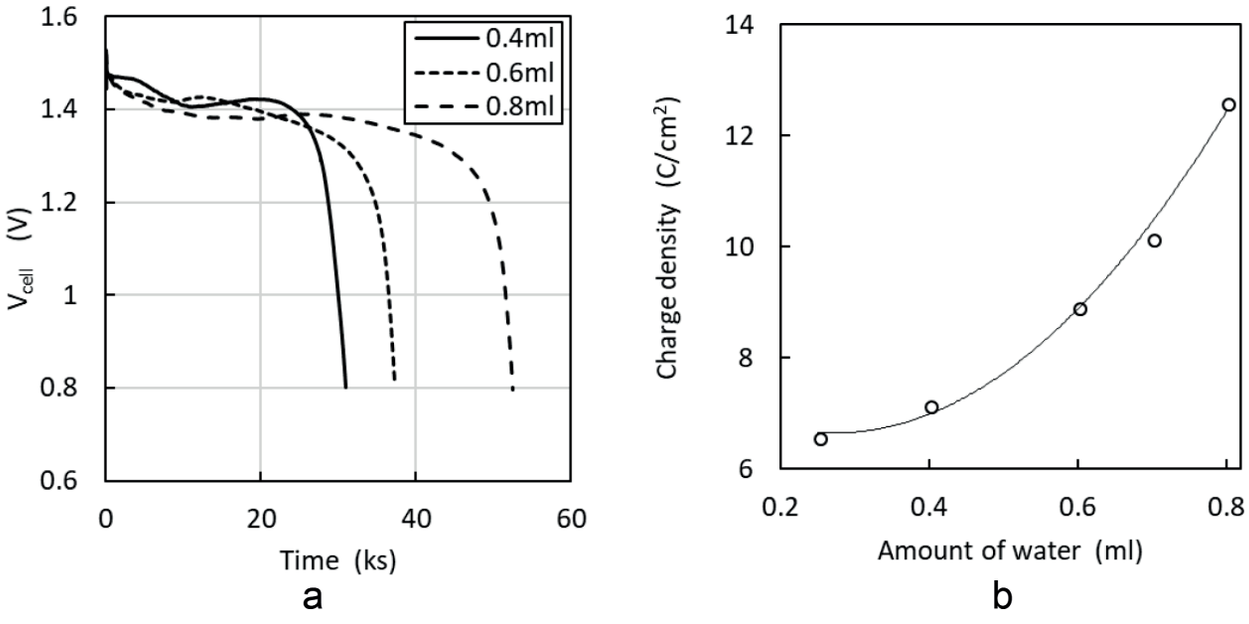


**Figure 5.** Discharge behavior of WAMB (unit cell) at the first injection of water at a current density of 0.24 mA/cm$^2$ [11]. (a) Discharge curves of WAMB. (b) Dependence of discharged period on the water content.

**Figure 6** presents the discharge behavior of WAMB with different discharge cycles [13]. $E_a$ kept constant about −1.6 V regardless of discharge time and cycles, and $E_c$ changed every discharge cycle. $V_{cell}$ followed the change in $E_c$. The discharge time was gradually shortened by injection cycles shown in **Figure 6(b)**. It was possible to regenerate WAMB up to 8 times of water injection. $t_{total}$ was calculated to be 51.7 h.

**Figure 7** exhibits the change of Nyquist diagram of the anode, cathode, and unit cell with different injection cycles. The Mg anode drew a depressed capacitive semicircle, followed by an inductive loop in the low frequency region. In general, the size of trajectory increased with injection cycles. The impedance of the cathode was negligible in the first cycle but increased thereafter. Furthermore, a Warburg impedance was recognized in the low frequency region.

There are several EIS studies on the corrosion of Mg or Mg alloys [14–16], but the application to neither Mg battery nor Mg anodized in NaCl solution is rare. Then, referring the equivalent electric circuit of pure Mg corroding in NaCl solution [14], a circuit for the WAMB anode is proposed in **Figure 8(a)** [13].

$R_{s.a}$: Solution resistance at the anode.

$R_{1a}$, $R_{2a}$: Resistance associated with the dissolution of the anode.

$R_{3a}$: Resistance associated with the hydrogen gas evolution on the anode.

$CPE_{1a}$: Constant phase element associated with the discharge product on the anode.

$CPE_{2a}$: Constant phase element associated with the electrochemical double layer of the anode.

$L_a$: Inductance associated with the dissolution of the anode.

As for the WAMB cathode, an equivalent circuit was expressed in **Figure 8(b)**, referring the $MnO_2$ electrode of Zn-$MnO_2$ battery [17, 18].

$R_{s.c}$: Solution resistance at the cathode.

$R_{ct.c}$: Resistance associated with the reduction of $MnO_2$.

$CPE_c$: Constant phase element associated with the electrochemical double layer of the cathode.

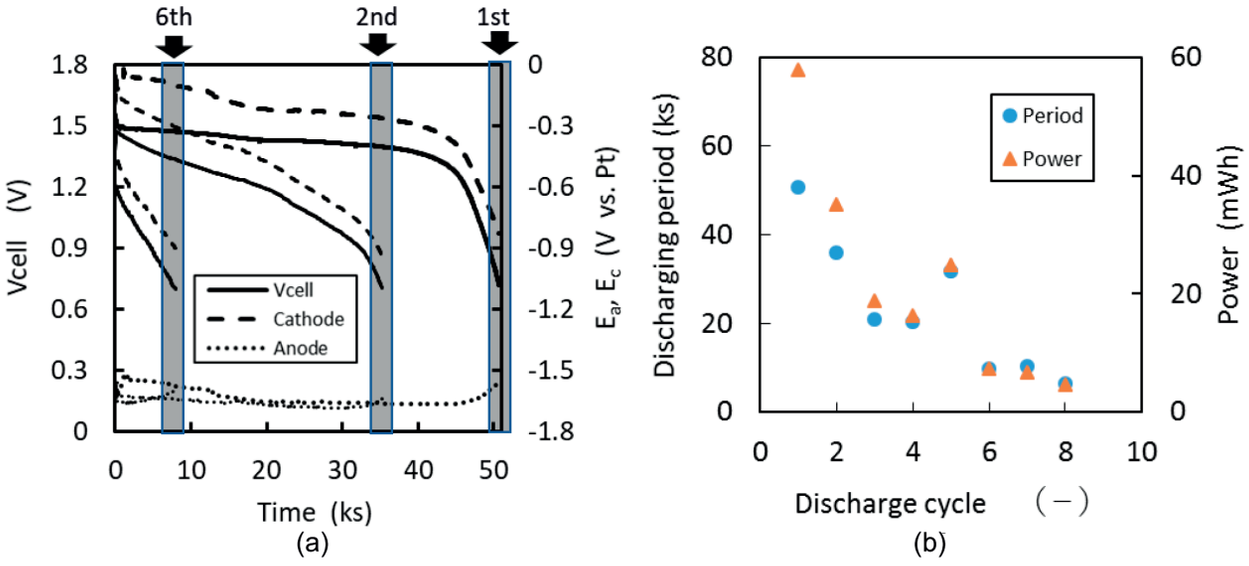


**Figure 6.** Discharge behavior of WAMB (unit cell) at a current density of 0.24 mA/cm² [13]. (a) Change of $E_a$, $E_c$, and $V_{cell}$ with time under different discharge cycle. (b) Change of discharge time and power with the discharge cycle.

$W_c$: Warburg impedance of the cathode (open).

Here, constant phase element (CPE) [19] such as $CPE_{1a}$, $CPE_{2a}$, and $CPE_c$ was employed instead of capacitance to reflect the inhomogeneity of the electrode surface.

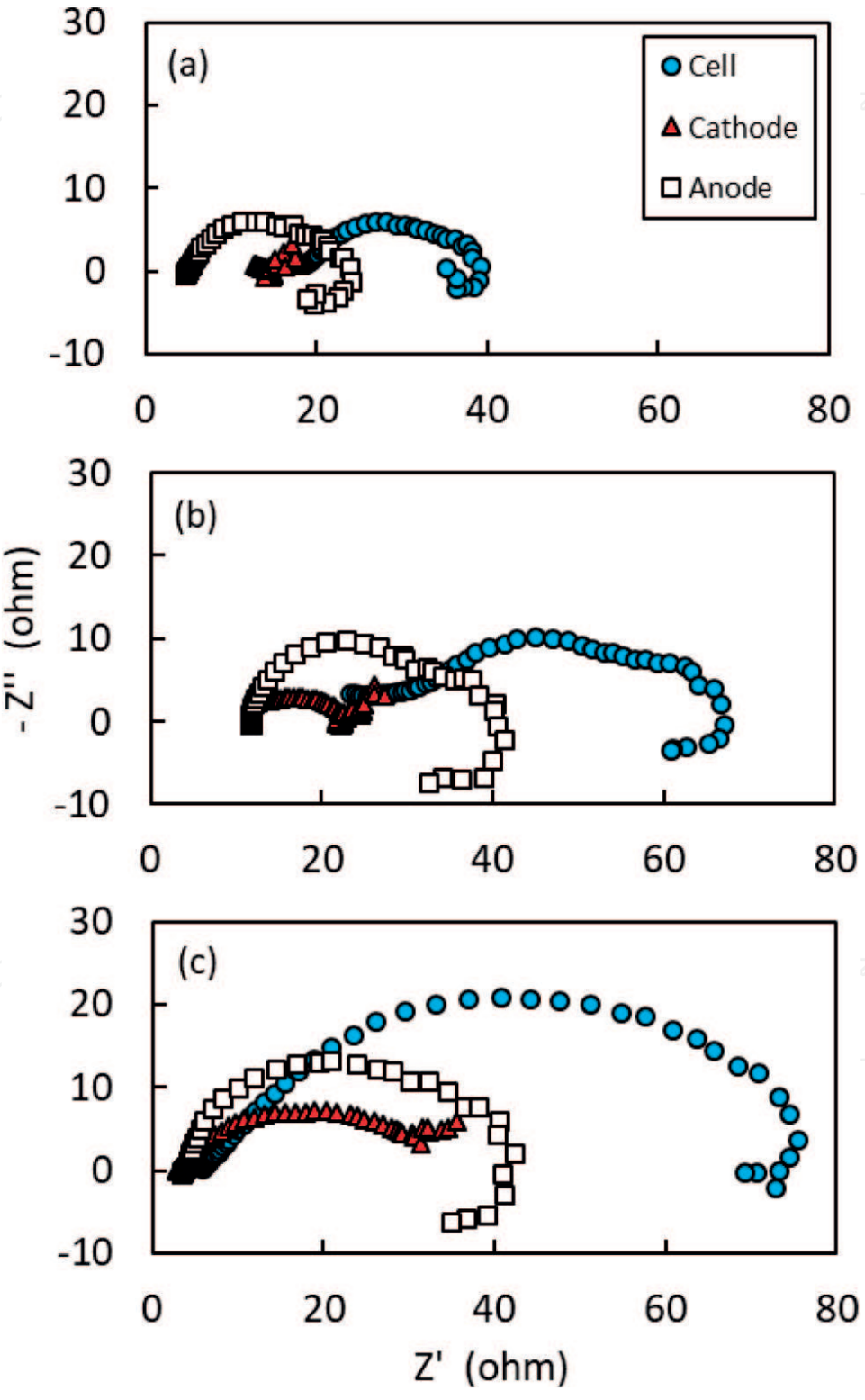


**Figure 7.** Nyquist diagrams of the anode, cathode, and cell of WAMB unit cell after (a) first, (b) second, and (c) sixth cycles of water injection [13].

http://dx.doi.org/10.5772/intechopen.79789

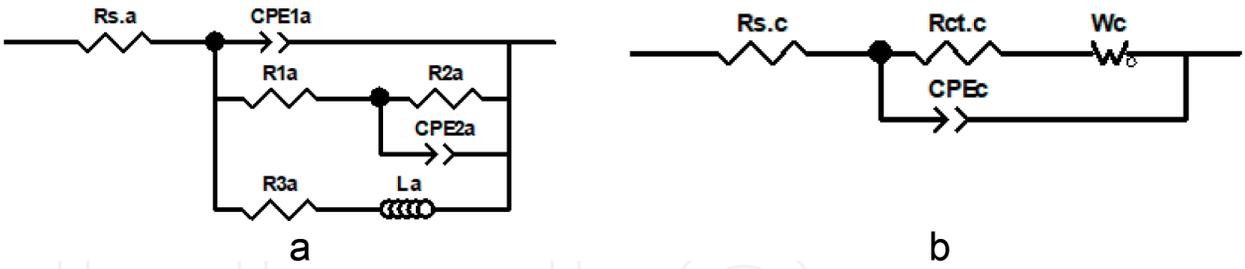


**Figure 8.** Electrical equivalent circuits for the WAMB anode and the WAMB cathode. (a) Anode. (b) Cathode.

| **Anode** | | | | | | | | | |
|---|---|---|---|---|---|---|---|---|---|
| | $R_{s.a}$ (Ω) | $R_{1a}$ (Ω) | $R_{2a}$(Ω) | $R_{3a}$ (Ω) | $CPE_{1a\text{-}T}$ (-) | $CPE_{1a\text{-}}$(-) | $CPE_{2a\text{-}T}$ (-) | $CPE_{2a\text{-}P}$ (-) | $L_a$ (Ωs) |
| First | 4.47 | 3E-07 | 23.3 | 27.2 | 3.74E-03 | 0.284 | 2.01E-04 | 0.84 | 4.17 |
| Second | 11.3 | 0.13 | 36.1 | 34.8 | 1.93E-03 | 0.424 | 9.13E-06 | 1.14 | 6.96 |
| Sixth | 3.05 | 3.72 | 36.5 | 58.7 | 4.01E-04 | 0.733 | 2.85E-06 | 1.25 | 12.9 |
| **Cathode** | | | | | | | | | |
| | $R_{s.c}$ (Ω) | $R_{ct.c}$ (Ω) | $CPE_{c\text{-}T}$ (-) | $CPE_{c\text{-}P}$ (-) | $W_{c\text{-}R}$ (-) | $W_{c\text{-}T}$ (-) | $W_{c\text{-}P}$ (-) | | |
| First | 12.3 | 1.71 | 8.99E-06 | 0.956 | 9.7 | 0.702 | 0.608 | | |
| Second | 11.6 | 10.3 | 2.90E-05 | 0.744 | 17.6 | 1.053 | 0.744 | | |
| Sixth | 2.24 | 25.7 | 4.49E-04 | 0.628 | 10.8 | 0.393 | 0.628 | | |

**Table 2.** Parameters of equivalent circuit shown in **Figure 8** to simulate the response of WAMB discharged at 0.24 mA/cm$^2$.

The curve fitting of the experimental data of each electrode was performed using simulation software. The results are shown in **Table 2** and superimposed on the experimental data in **Figure 9**. The proposed circuit approximated the impedance spectrum, showing the depressed capacitive semicircle, the presence of the inductive loop at the anode, and the Warburg impedance at the cathode. Curioni et al. [15] reported that the reciprocal of ($R_{1a}$ + $R_{2a}$) shows a good correlation with the corrosion rate of pure Mg obtained from the hydrogen evolution reaction. Then, the parameter ($R_{1a}$ + $R_{2a}$) is replaced with $R_{ct.a}$, the sum of $R_{ct.a}$ and $R_{ct.c}$. is replaced with $R_{ct.cell}$, and discussed herewith. These parameters and $R_s$ at each electrode can be obtained roughly from the trajectory shown in **Figure 9** [14].

**Figure 10** plots the time dependence of $R_s$ and $R_{ct}$ of the anode, cathode, and cell at different injection cycles. In general, $R_s$ increases with the discharge time, suggesting a decrease in the water content in the cell. However, at the sixth water injection, $V_{cell}$ reached the terminal voltage before $R_s$ started to increase. In case of $R_{ct}$, the cathode took a smaller value at the initial stage than the anode. After that, both values increased with the number of water injections. In the sixth water injection, $R_{ct.a}$ and $R_{ct.c}$ reached the same level.

**Figure 11** presents the potentiodynamic polarization curves of the cathode before and after the discharge test. The cathode current decreased significantly after the test, suggesting a decrease in discharge capacity. In case of the anode, a white-gray discharge product was observed. After removing them, the thickness of the Mg plate was partly diminished, but the shape remained.

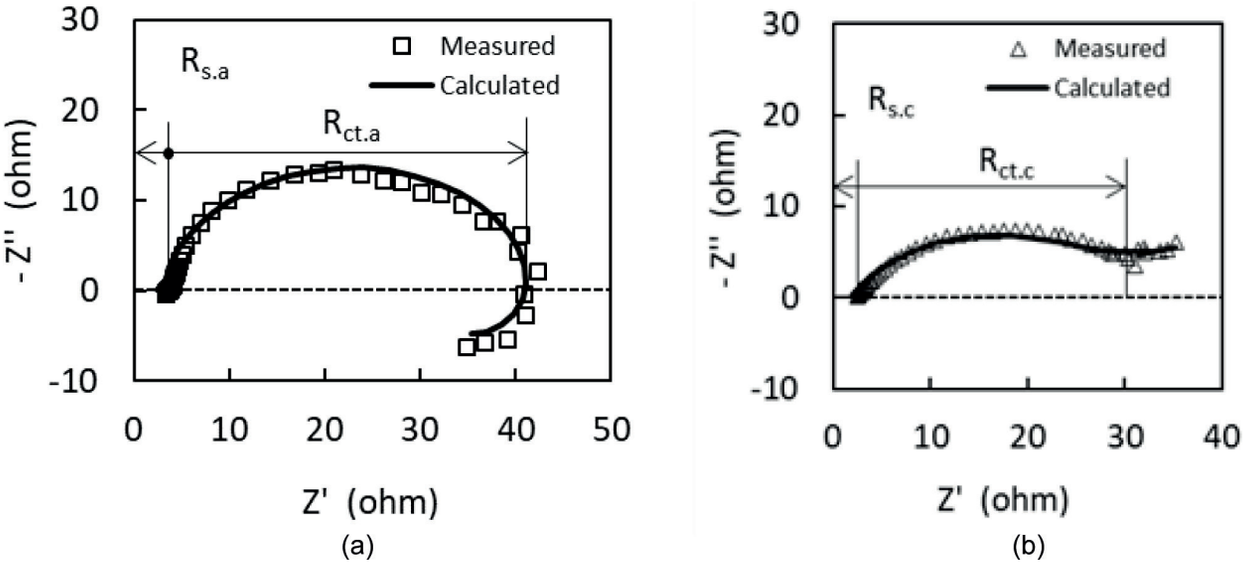


**Figure 9.** Comparison between the calculated and the measured impedance spectra of WAMB. (a) Anode after 6th cycle. (b) Cathode after 6th cycle.

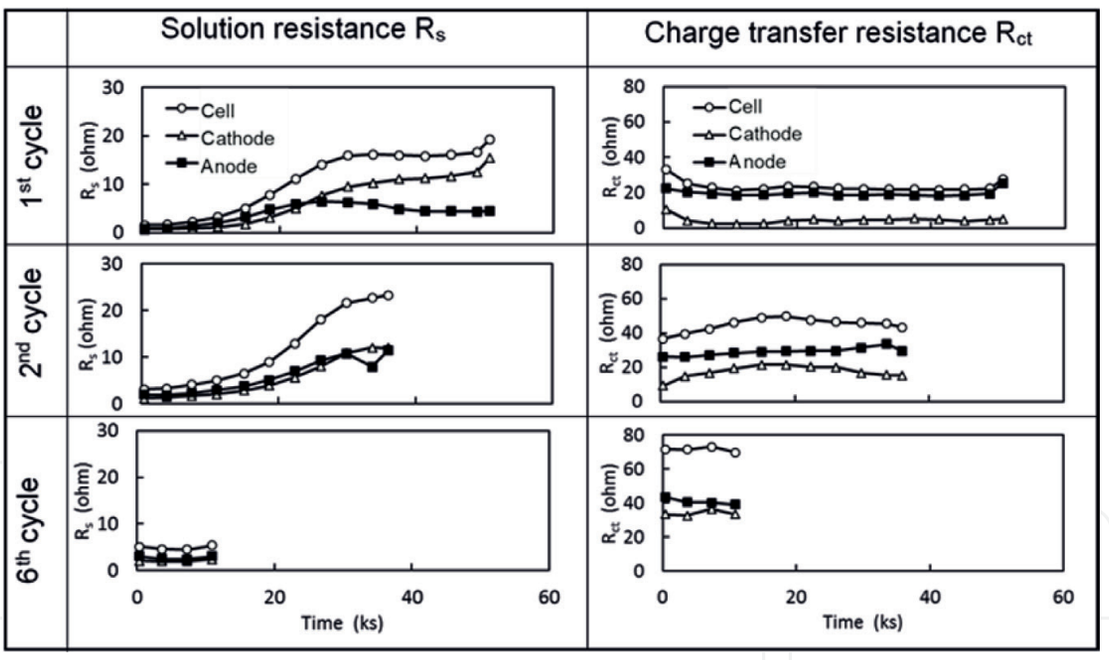


**Figure 10.** Time dependence of $R_s$ and $R_{ct}$ of the WAMB cathode and the WAMB anode and their combined cell (unit cell) at a current density of 0.24 mA/cm$^2$.

### 3.3. Discharge behavior of stacked cell with water injection

Time variation of $V_{cell}$ of the stacked WAMB at a current density of 0.24 mA/cm$^2$ was presented in **Figure 12**. As expected, $V_{cell}$ has quadrupled by stacking four unit cells. The behavior of $V_{cell}$ was basically the same as that of the unit cell. Total discharge time reached 95.6 h, which was about twice that of the unit cell. **Figure 13** shows the Nyquist diagram of the stacked

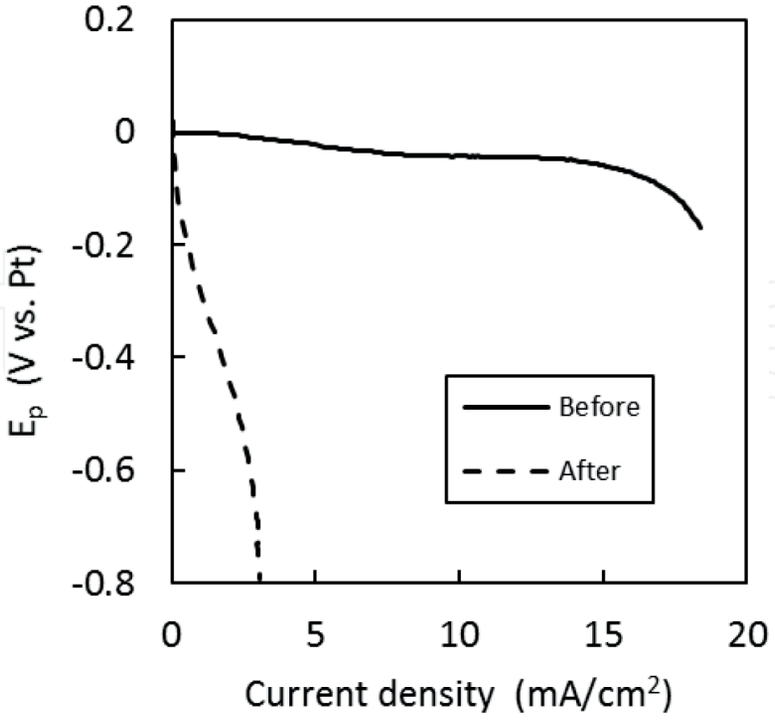


**Figure 11.** Potentiodynamic polarization curves of the WAMB cathode (unit cell) before discharging and after six cycles of discharging.

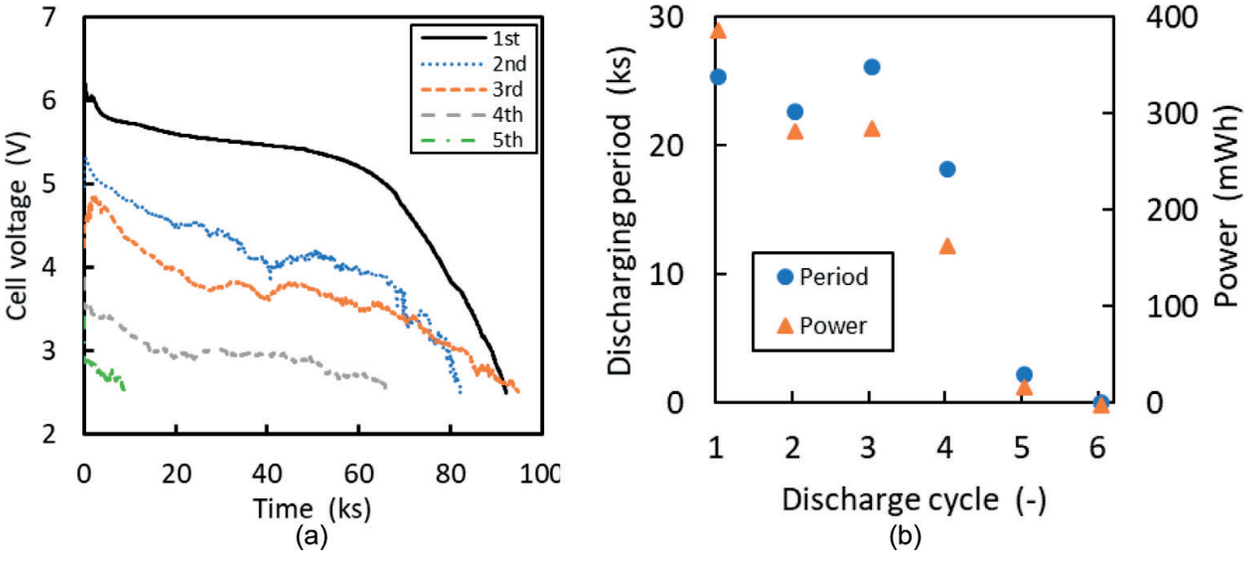


**Figure 12.** Discharge behavior of the WAMB stacked cell at a current density of 0.24 mA/cm$^2$. (a) Discharge curves. (b) Change of discharge time and power with discharge cycle.

cell after the first, third, and fifth water injections. The spectra drew depressed capacitive semicircles up to the fourth water injection. The diameter (= $R_{ct.cell}$) was initially large, but gradually became smaller. In the fifth water injection, a Warburg impedance appeared in the low frequency region. $R_{s.\ cell}$ and $R_{ct.cell}$ at the terminal voltage were 24 and 288 Ω, respectively, which were about four times the value in the unit cell.

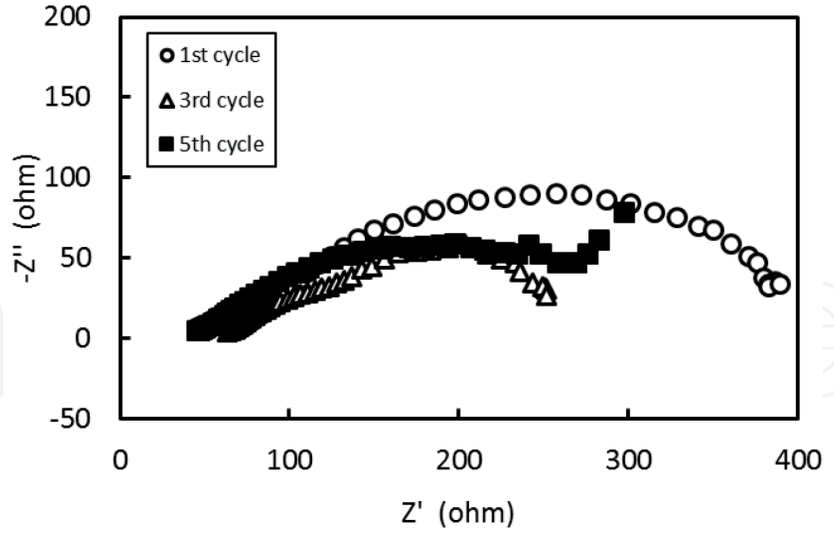


**Figure 13.** Impedance spectra of WAMB (stacked cell) at the termination voltage after different discharging cycles.

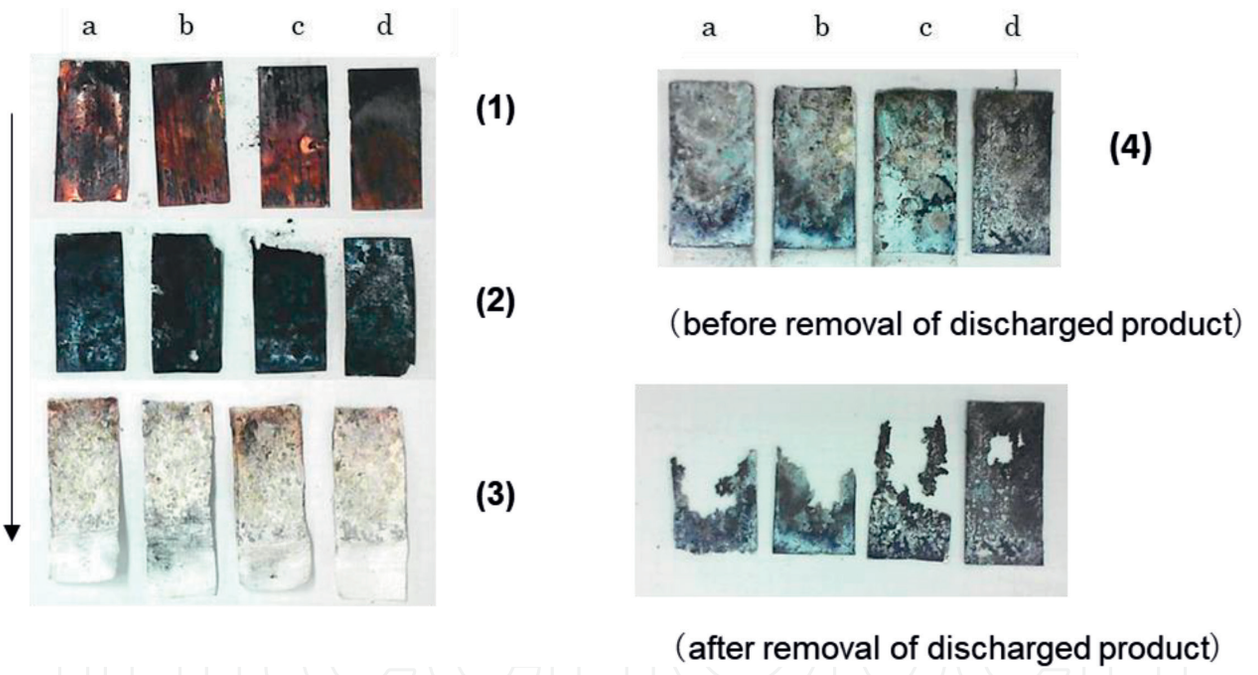


**Figure 14.** Appearance of WAMB (stacked cell) at a current density of 0.24 mA/cm$^2$ after six cycles of discharge [13].

### 3.4. Discharge capacity and current efficiency

The appearance of the electrode after the discharge test was shown in **Figure 14**. They are: (1) current collector, (2) cathode, (3) separator, and (4) anode before/after the removal of the discharge product. The alphabetical suffix indicates the layer of the stacked cell. Thus, the first unit cell was stacked in the order of *[a1/a2/a3/b4]*, following the second cell as *[b1/b2/b3/b4]*, the third as *[c1/c2/c3/c4]*, and the fourth as *[d1/d2/d3/d4]*. At the anode, a white and gray discharge product was visible. After the removal of the product, more than half of the anode

http://dx.doi.org/10.5772/intechopen.79789

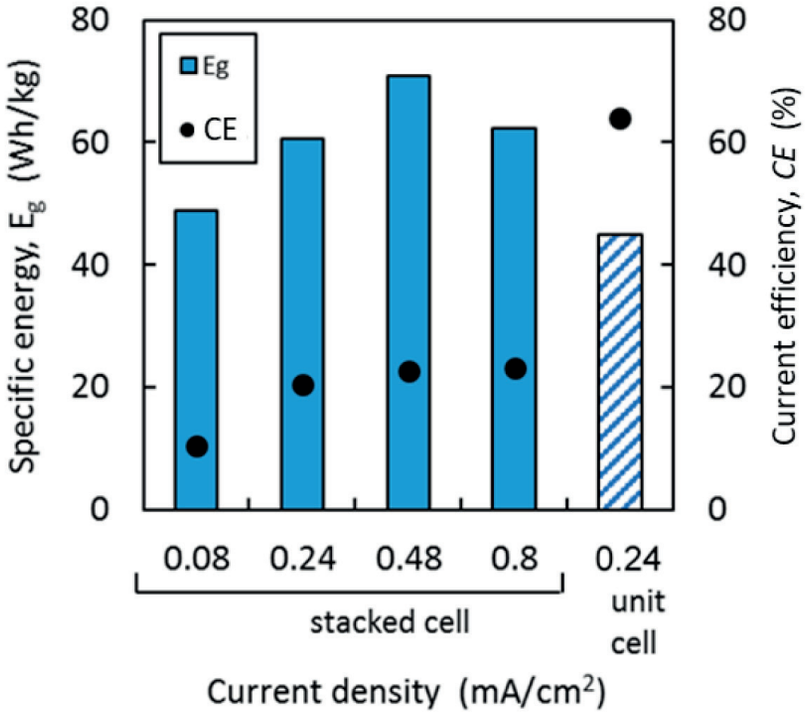


**Figure 15.** Specific energy and current efficiency of WAMB [13].

was disappeared except for the *d4*, which was located on the outermost side of the stacked cell. The surface of the Cu current collector attached to the Mg anodes was blackened.

**Figure 15** illustrates the energy density $E_g$ and the current efficiency *CE* of the unit, and the stacked cell. $E_g$ reached its maximum of 71 Wh/kg at $i_d$ of 0.48 mA/cm$^2$. It is noticeable that *CE* was greatly decreased by stacking the unit cells.

## 4. Discussions

### 4.1. Discharge behavior of WAMB unit cell

Discharging of WAMB begins with feeding water to the cathodes via separators. Water dissolves NaCl in the cathode material and creates an ionic path between the electrodes. The cell reactions are expressed as:

$$\text{Anode}: Mg \rightarrow Mg^{2+} + 2e \tag{4}$$

$$\text{Cathode}: 2MnO_2 + H_2O + 2e \rightarrow Mn_2O_3 + 2OH^- \tag{5}$$

$$\text{Total}: Mg + 2MnO_2 + H_2O \rightarrow Mn_2O_3 + Mg(OH)_2 \tag{6}$$

Eq. (6) is an exothermic reaction. Enthalpy change $-\Delta H$ was calculated to be 484 kJ/mol [20]. Since WAMB is an open structure, the injected water evaporates gradually due to heat. Water was also consumed by Eq. (5) to form $Mg(OH)_2$. Therefore, intermittent water injection is indispensable. The discharge behavior of WAMB depends on the dissolution of the Mg anode and the reduction of $MnO_2$ in the cathode. As shown in **Figure 6**, $E_a$ was stable regardless of the discharge time and the cycle of water injection. In contrast, $E_c$ varied with discharge conditions that affected $V_{cell}$. All these facts suggest that WAMB is the cathode-controlled system. The decline in the cathode capacity after the discharge shown in **Figure 11** confirms such an assumption.

Based on the EIS result shown in **Figure 10**, the anode and cathode behaviors during the discharge can be schematically interpreted as **Figure 16**. At the initial stage, $R_{ct.c}$ is smaller than $R_{ct.a}$ and does not affect the discharge behavior. As time elapses, $R_{s.cell}$ gradually increases due to the depletion of water and stops the discharge reaction. After repeated water injection, the initial $R_{ct.c}$ and $R_{ct.a}$ tend to show larger values than the preceding cycle. This suggests a decrease in the conductive $MnO_2$ in the cathode and a decrease in the reaction area of the anode due to the accumulation of $Mg(OH)_2$. In addition, a decrease in $E_c$ lowers $V_{cell}$. At the end of the period, even if the water amount is sufficient (small $R_{s.cell}$), the gap between $V_{cell}$ and the terminal voltage becomes small, so the discharge ends in a short time.

At the terminal stage, the Warburg impedance appeared in the cathode of **Figure 7(b)** and **(c)**. Qu [18] discussed the existence of Warburg impedance appearing at the $MnO_2$ cathode of an alkaline Mn battery system, in terms of the volume expansion of the cathode during discharge. Such expansion prevents the proton diffusion of the entire lattice of $MnO_2$, which is an important rate-determining step. When the discharge exceeds 50%, the localized Jahn-Teller deformation begins to occur and the proton diffusion coefficient decreases. Though such volume expansion was not recognizable in the present system, structural analysis of the cathode using XRD would provide detailed mechanism of the degradation of WAMB.

### 4.2. Discharge behavior of WAMB stacked cell

In general, the discharge behavior of the stacked cell follows that of the unit cell. It is worth noting that $t_{total}$ almost doubled by stacking. The exact cause is not clear, but it may be related to the generation of the voluminous $Mg(OH)_2$ which is 73.5% more molar volume than Mg metal [21]. Such expansion compresses the electrodes in the casing, improves mutual contact, and would lead to the prolongation of the discharge time.

On the other hand, *CE* was sharply decreased in the stacked cell. *CE* of 64% obtained at the unit cell is within the range of 55–66%, which is reported in the corrosion of Mg [22]. The reason that the *CE* of Mg is less than 100% in Mg is closely related to the hydrogen gas evolution reaction that occurs simultaneously even if Mg is anodically polarized [23, 24].

$$2H_2O + 2e \rightarrow H_2 + 2OH^- \quad (7)$$

However, the fact is that *CE* as low as 20% in the stacked cell cannot be explained in this context. The reason for this is interpreted by galvanic corrosion by the Cu current collector, which

is illustrated in **Figure 17** [13]. During water injection, most of the water penetrates from the separator into the cathode material osmotically. However, some of them may penetrate small gaps between the Cu collector and the Mg anode. As a result, a galvanic cell having Mg as anode and Cu as cathode is formed, and the former is corroded preferentially. In this case, the anode reaction is represented by Eq. (4) and the cathode reaction is by Eq. (7). In principle, WAMB establishes the flows of electron and ions ($OH^-$) and generates electricity as shown in Section (a) of **Figure 17**. However, the portion where the galvanic corrosion is being occurred forms the closed circuit shown in section (b), and the Mg anode does not contribute to the discharge performance and is wasted by corrosion. The fact that the Mg anode *d4* in **Figure 14** is less susceptible to corrosion than other anodes corroborates the absence of such galvanic corrosion. In addition, galvanic corrosion results in forming the corrosion products between the anode and the Cu collector, causing IR drop and reducing $V_{cell}$. Cu collectors are also oxidized (see **Figure 14**—(1)) to increase the contact resistance. To reduce the loss due to galvanic corrosion and maximize the discharge capacity of WAMB, the choice of higher $i_d$ up to around 0.5 mA/cm$^2$ is recommended.

### 4.3. Technical challenge and future applications of WAMB

Based on current research, the gravimetric energy density $E_g$ of WAMB is 71 kWh/kg, which is inferior to Zn-alkaline $MnO_2$ battery (154 Wh/kg) or Zn-air battery (415 Wh/kg) [25]. Since WAMB inherits the dry Mg-$MnO_2$ battery or the reserved battery technologies [2, 3], of which $E_g$ is less than 100 Wh/kg [25], dramatic improvement of WAMB may not be feasible. Still, there are several rooms to enhance the capabilities of WAMB.

**A.** Design to eliminate galvanic corrosion in the stacked cell.

**B.** Catalyst for enhancing the ability of the cathode [26–30].

**C.** Mg alloy for improving discharge capacity [31–33].

**D.** Selection of electrolyte and additive [34–37].

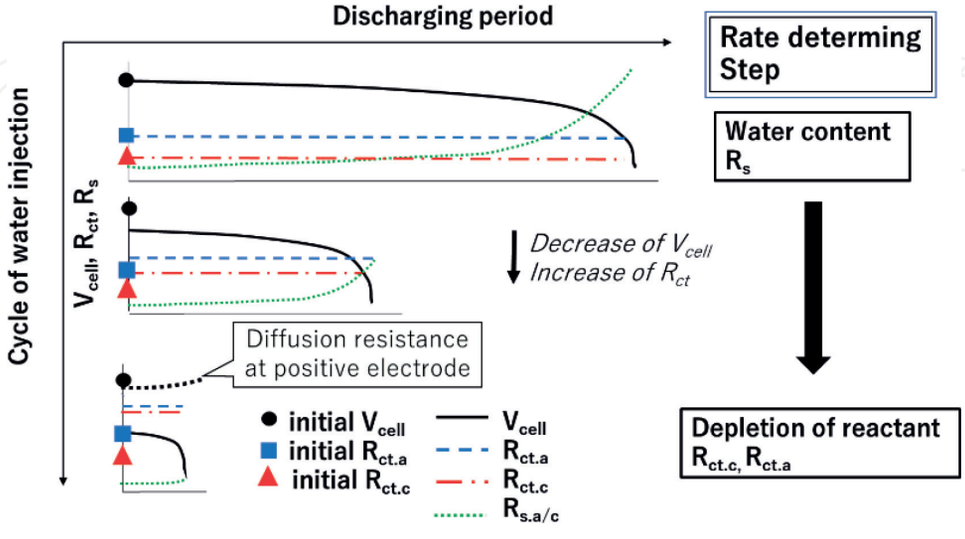


**Figure 16.** Schematic diagram of the time variation of electrochemical parameters in WAMB [13].

They are briefly commented as follows. Several studies conducted in type I water-activated Mg battery are also useful for type II WAMB. In addition, we performed some experimental trials that are summarized in **Table 3**. The relative increase in $t_{total}$ compared to the standard condition was used as an index of improvement.

*4.3.1. Design for eliminating galvanic corrosion in the stacked cell*

The galvanic corrosion occurs in the condition of stacking unit cells, and it seems that the penetration water in the gap between the anode and the Cu collector is the main cause. It is conceivable to separate the unit cells and connect them outside the casing to avoid the galvanic contact. Although it is technically possible, the structure becomes complicated. A solution is to bond the electrodes using conductive tape to seal the gap. Although it induces contact resistance to decrease $V_{cell}$, it is effective to eliminate the galvanic corrosion and improve the *CE*. With this configuration, a 150% increase in $t_{total}$ was possible in our preliminary trials.

*4.3.2. Catalyst for enhancing the ability of the cathode*

Eq. (5) can be considered as a kind of oxygen reduction reaction. Therefore, the addition of oxygen catalyst shifts $E_c$ more noble. Apart from Pt group catalysts, several organic [26, 27], inorganic [28], or complex [29, 30] catalysts are promising. We studied the effect of Ni, Cu, and Fe powder in the $MnO_2$ containing cathode mix. The addition of Ni powder gave the best performance among them.

*4.3.3. Mg alloy for improving discharge capacity*

In this study, a versatile AZ31 alloy was used as the anode. There are several Mg alloys developed for type I water-activated Mg batteries. It is effective to improve the discharge capacity

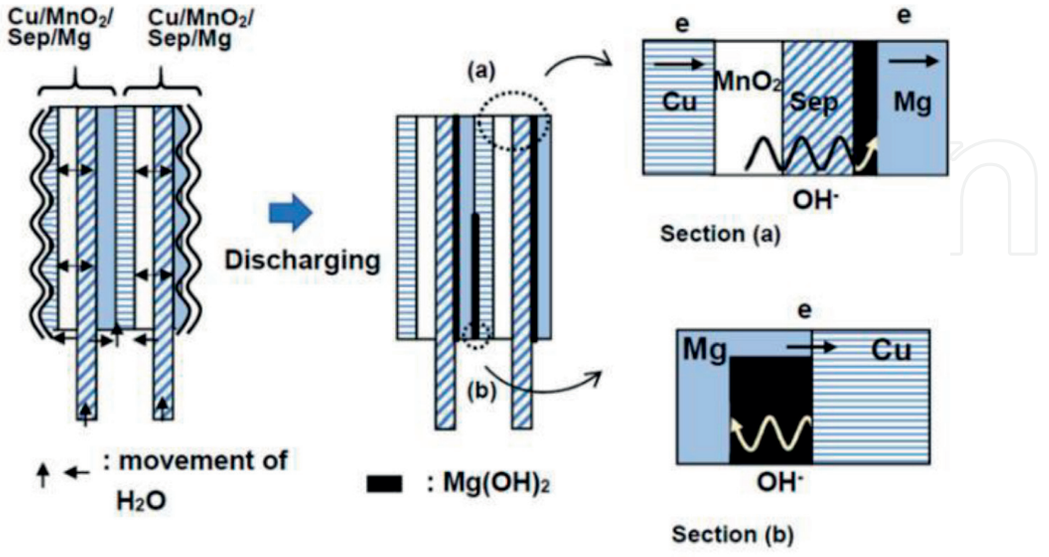


**Figure 17.** Schematic diagram of electron and ionic flows of WAMB (stacked cell): Section (a) indicates the normal discharge behavior, and section (b) indicates the abnormal behavior caused by the occurrence of a galvanic corrosion between the Cu current collector and the Mg anode.

| Method | Modification | Cell | $t_{total}$ (%) |
|---|---|---|---|
| A | Cu plated conductive tape bet. Mg/Cu | Stack | 146 |
| B | Add Cu powder in cathode mix | Stack | 82 |
| | Add Ni powder in cathode mix | Stack | 135 |
| | Add Fe powder in cathode mix | Stack | 105 |
| C | Use Mg-Li-Al alloy as anode | Unit | 208 |
| D | Add LiCl in cathode mix | Stack | 163 |
| — | None | — | 100 |

**Table 3.** Technical proposals to improve the discharge performance of WAMB.

by adding specific alloying elements such as Li [31], Ca [32], Pb [33] to Mg-Al alloys. As shown in **Table 3**, it was found that Mg-14Li-1Al alloy demonstrated excellent performance as the anode. The presence of lithium hydroxide in the discharge product seems to maintain $R_{s.a}$ low even after multiple water injections. Similar effects are expected for Mg-Al alloys containing Ca [32].

*4.3.4. Selection of electrolyte and additive*

NaCl is the standard electrolyte for type I and II water-activated batteries. It results in a larger $V_{cell}$ compared to a phosphate- or nitrate-based electrolyte but lowers *CE* [34]. Magnesium forms a soluble compound with organic acids such as acetic acid and citric acid [35]. Addition of citric acid did not improve the discharge performance of type I battery [36]. Some additives form chelates with Mg which raise $V_{cell}$ [37]. We found that the use of LiCl instead of NaCl increased $t_{total}$. Although the reason is uncertain, there is a possibility that the same effect as the Mg-Li-Al alloy anode described above may have occurred.

Finally, we consider that the recent attention of WAMB comes from aspects other than power-oriented issues, that is, the convenience and safe handling, or expectations of Mg as an energy carrier for a sustainable society [38]. Apart from LED lamps, water sensors from diapers [39] to underground pipelines [40], biodegradable batteries for medical implants or home appliances [41, 42] can be expected as new applications of WAMB.

## 5. Conclusions

A water-activated magnesium battery (WAMB) consisting of $MnO_2$ cathode and magnesium anode was evaluated. The obtained results are as follows:

1. The initial power density of WAMB showed the maximum of 10 mW/cm$^2$ at 15 mA/cm$^2$. The cell voltage under a constant current discharge of 0.24 mA/cm$^2$ was 1.4–1.5 V over 50 h at the unit cell. Changes in the cell voltage were closely related to the performance of the cathode. The injection of water regenerated the WAMB unit cell up to 8 times.

2. Electrochemical impedance spectroscopy was applied to monitor the discharge performance of WAMB. An electrical equivalent circuit of the anode and the cathode was proposed from the frequency spectra. They consisted of solution resistance, charge transfer resistance, constant phase element, inductance for the anode, and Warburg impedance for the cathode. Curve fitting using simulation software agreed well the experimental data.

3. By monitoring solution resistance and charge transfer resistance, the degradation behavior of WAMB was analyzed. At the initial stage, an increase of solution resistance due to the depletion of water determined the discharge time. When water was repeatedly injected to regenerate WAMB, the increase in the charge transfer resistance of the anode and the cathode controlled the discharge time and the cell voltage, respectively. At the final stage, the Warburg impedance appeared in the cathode frequency spectrum. These data suggest that WAMB is the cathode-controlled system. The loss of discharge capacity and the volume expansion of $MnO_2$ was considered.

4. Stacking the unit cells in series was effective for increasing the cell voltage and extending the discharge time. On the other hand, the current efficiency decreased from 64 to 10–20%. The reason was interpreted in terms of a galvanic corrosion occurring at the Mg anode and the Cu current collector.

5. The power density of WAMB was 71 Wh/kg, which was lower than the current Zn batteries. Several approaches to improve performance were proposed. Promising applications of WAMB including biodegradable batteries were also mentioned.

## Author details

Isao Nakatsugawa[1]*, Yasumasa Chino[1] and Hideki Nakano[2]

*Address all correspondence to: i.nakatsugawa@aist.go.jp

1 Structural Materials Research Institute, National Institute of Advanced Industrial Science and Technology, Nagoya, Japan

2 CLT Ltd., Nagoya, Japan

## References

[1] Wang N, Wang R, Peng C, Hu C, Feng Y, Peng B. Research progress of magnesium anodes and their applications in chemical power sources. Transactions of the Nonferrous Metals Society of China. 2014;**242**:427-2439. DOI: 10.1016/S1003-6326(14)63367-7

[2] Spellman PJ. Magnesium and aluminum batteries. In: Reddy T, editor. Linden's Handbook of Batteries. 4th ed. New York: McGraw-Hill Education; 2011. pp. 10.1-10.13

[3] Lucero RD, Karpinski AP. Reserve Magnesium Anode and Zinc/Silver Oxide Batteries. In: Reddy T, editor. Linden's Handbook of Batteries. 4th ed. New York: McGraw-Hill Education; 2011. pp. 34.1-34.7

[4] Saha P, Datta MK, Velikokhatnyi OI, Manivannan A, Alman D, Kumta PR. Rechargeable magnesium battery: Current status and key challenges for the future. Progress in Materials Science. 2014;**66**:1-86. DOI: 10.1016/j.pmatsci.2014.04.001

[5] Yoo HD, Shterenberg I, Gofer Y, Gershinsky G, Pour N, Aurbach D. Mg rechargeable batteries: An on-going challenge. Energy & Environmental Science. 2013;**6**:2265-2279. DOI: 10.1039/C3EE40871J

[6] Zhang T, Tao Z, Jun C. Magnesium-air batteries: From principle to application. Materials Horizons. 2014;**1**:196-206. DOI: 10.1039/c3mh00059a

[7] Ito A, Abe H, Kubota M, Taira Y, Iizuka H, Saito K, Takahara T, Ono Y. Evaluation test of magnesium air battery 'Mg box' for emergencies. FB Technical News. 2014;**70**:23-27

[8] Suzuki S. JP Patent No. 519613, WO2013/018769

[9] Aqumo Candle [Internet]. 2017. Available from: http://www.aqumo-holdings.com [Accessed: May 24, 2018]

[10] Aqumo Candle [Internet]. 2015. Available from: https://www.youtube.com/watch?v=xQxf5Ff7cQ4 [Accessed: May 24, 2018]

[11] Nakatsugawa I, Suzuki S. Discharge behavior of water activated magnesium-air battery. In: Proceedings of 130th Japan Institute of Light Metals; 2016. p. 16

[12] Nakatsugawa I, Nakano H. Discharge behavior of water-activated magnesium battery. In: Proceedings of 131st Japan Institute of Light Metals; 2016. p. 44

[13] Nakatsugawa I, Nakano H. Discharge behavior of water-activated magnesium battery. Journal of Japan Institute of Light Metals. 2017;**67**:503-510

[14] King AD, Birbilis N, Scully JR. Accurate electrochemical measurement of magnesium corrosion rates; a combined impedance, mass-loss and hydrogen collection study. Electrochimica Acta. 2014;**121**:394-406. DOI: 10.1016/j.electacta.2013.12.124

[15] Curioni M, Scenini F, Monetta T, Bellucci F. Correlation between electrochemical impedance measurements and corrosion rate of magnesium investigated by real-time hydrogen measurement and optical imaging. Electrochimica Acta. 2015;**166**:372-384. DOI: 10.1016/j.electacta.2015.03.050

[16] Feliu S Jr, El Hadad AA, Barranco V, Llorente I, García-Galván FR, Jiménez-Morales A, Galván JC. Native oxide films on AZ31 and AZ61 commercial magnesium alloys—Corrosion behaviour, effect on isothermal oxidation and sol–gel thin film formation. In: Ahmaz Z, editor. New Trends in Alloy Development, Characterization and Application. Rijeka: IntechOpen; 2015. pp. 97-123. DOI: 10.5772/60721

[17] Mekhalfi H, Chelali N, Benhamimid S, Bahloul A. Recycling of manganese dioxide from spent Zn–$MnO_2$ cells. Russian Journal of Applied Chemistry. 2015;**88**:879-884. DOI: 10.1134/S1070427215050249

[18] Qu D. Application of a.c. impedance technique to the study of the proton diffusion process in the porous $MnO_2$ electrode. Electrochimica Acta. 2003;**48**:1675-1684. DOI: 10.1016/S0013-4686(03)00146-4

[19] Orazem ME, Tribollet B. Electrochemical Impedance Spectroscopy. New Jersey: Wiley; 2017. pp. 395-418

[20] The Chemical Society of Japan, editors. Handbook of Chemistry. Pure Chemistry. 4th ed. Vol. II-285. Tokyo: Maruzen; 1993

[21] Song G. Corrosion electrochemistry of magnesium and its alloys. In: Song G, editor. Corrosion of Magnesium Alloys. Cambridge: Woodhead Publishing; 2011. p. 12

[22] Glicksmann R. Anodic dissolution of Magnesium alloys in aqueous salt solutions. Journal of the Electrochemical Society. 1959;**106**:83-88. DOI: 10.1149/1.2427299

[23] Frankel GS, Samaniego A, Birbilis N. Evolution of hydrogen at dissolving magnesium surfaces. Corrosion Science. 2013;**70**:104-111. DOI: 10.1016/j.corsci.2013.01.017

[24] Cano ZP, Kish JR, McDermid JR. On the evolution of cathodic activity during corrosion of magnesium alloy AZ31B in a dilute NaCl solution. Journal of the Electrochemical Society. 2016;**163**:C62-C68. DOI: 10.1149/2.0151603jes

[25] Linden D, Reddy TB. Basic concepts. In: Reddy T, editor. Linden's Handbook of Batteries. 4th ed. New York: McGraw-Hill Education; 2011. pp. 1.3-1.17

[26] Shu C, Wang E, Jiang L, Shu SGC. High performance cathode based on carbon fiber felt for magnesium-air fuel cells. International Journal of Hydrogen Energy. 2013;**38**: 5885-5893. DOI: 10.1016/j.ijhydene.2013.02.093

[27] Yang D, Bhattacharjya D, Inamdar S, Park J, Yu J. Phosphorus-doped ordered mesoporous carbons with different lengths as efficient metal-free electrocatalysts for oxygen reduction reaction in alkaline media. Journal of the American Chemical Society. 2012;**134**:16127-16130. DOI: 10.1021/ja306376s

[28] Gorlin Y, Jaramillo TF. A bifunctional nonprecious metal catalyst for oxygen reduction and water oxidation. Journal of the American Chemical Society. 2010;**132**:13612-13614. DOI: 10.1021/ja104587v

[29] Wu Z, Yang S, Sun Y, Parvez K, Feng X, Müllen K. 3D nitrogen-doped graphene aerogel-supported $Fe_3O_4$ nanoparticles as efficient electrocatalysts for the oxygen reduction reaction. Journal of the American Chemical Society. 2012;**134**:9082-9085. DOI: 10.1021/ja3030565

[30] Milusheva YD, Boukoureshtlieva RI, Hristov SM, Kaisheva AR. Environmentally-clean Mg-air electrochemical power sources. Bulgarian Chemical Communications. 2011;**43**:42-47

[31] Cao D, Wu L, Sun Y, Wang G, Lu Y. Electrochemical behavior of Mg–Li, Mg–Li–Al and Mg–Li–Al–Ce in sodium chloride solution. Journal of Power Sources. 2008;**177**:624-630. DOI: 10.1016/j.jpowsour.2007.11.037

[32] Yuasa M, Huang X, Suzuki K, Mabuchi M, Chino. Discharge properties of Mg-Al-Mn-Ca and Mg-Al-Mn alloys as anode materials for primary magnesium-air batteries. Journal of Power Sources. 2015;**297**:449-456. DOI: 10.1016/j.jpowsour.2015.08.042

[33] Wang N, Wang R, Peng C, Peng B, Feng Y, Hu C. Discharge behaviour of Mg-Al-Pb and Mg-Al-Pb-In alloys as anodes for Mg-air battery. Electrochimica Acta. 2014;**149**:193-205. DOI: 10.1016/j.electacta.2014.10.053

[34] Richey FW, McCloskey BD, Luntz A. Mg anode corrosion in aqueous electrolytes and Implications for Mg-air batteries. Journal of the Electrochemical Society. 2016;**163**:A958-A963. DOI: 10.1149/2.0781606jes

[35] Nwaogu UC, Blawert C, Scharnagl N, Dietzel W, Kainer U. Effects of organic acid pickling on the corrosion resistance of magnesium alloy AZ31 sheet. Corrosion Science. 2010;**52**:2143-2154. DOI: 10.1016/j.corsci.2010.03.002

[36] Yasuda T, Yamazaki T, Honbo E, Takata K, Ishikubo T, Takatsuji N. Development of Magnesium Fuel Cell, Collection of Academic Papers of Toyama New Industry Organization. Toyama: 2013. pp. 26-33

[37] Höche D, Sviatlana L, Zheludkevich ML. Electrolyte additives for magnesium air batteries. European Patent. EP20160187152

[38] Garra P, Leyssens G, Allgaier O, Schönnenbeck C, Tschamber V, Brilhac JF, Tahtouh T, Guézet O, Allano S. Magnesium/air combustion at pilot scale and subsequent PM and $NO_x$ Emissions. Applied Energy. 2017;**189**:578-587. DOI: 10.1016/j.apenergy.2016.12.069

[39] Sherron M. Smart diaper. US patent. US20100241094A1

[40] Bhatti M, Reyzin I, Enzinna D. Leak detection apparatus for liquid circulation cooling system. US patent. US6826948 B1

[41] Tsang M, Armutlulu A, Martinez A, Herrault F, Allen SAB, Allen MG. A MEMS-enabled biodegradable battery for powering transient implantable devices. In: 2014 IEEE 27th International Conference on MEMS; 2014. pp. 358-361. DOI: 10.1109/MEMSYS.2014.6765650

[42] Edupuganti V, Solanki R. Fabrication, characterization, and modeling of a biodegradable battery for transient electronics. Journal of Power Sources. 2016;**336**:447-454. DOI: 10.1016/j.jpowsour.2016.11.004

IntechOpen